An experimentally validated and parameterized periodic unit-cell reconstruction of open-cell foams

P. De Jaeger,[1,2,a)] C. T'Joen,[1,3] H. Huisseune,[1] B. Ameel,[1] and M. De Paepe[1]
[1]*Department of Flow, Heat and Combustion Mechanics, Ghent University, Sint-Pietersnieuwstraat 41, 9000 Ghent, Belgium*
[2]*NV Bekaert SA, Bekaertstraat 1, 8500 Zwevegem, Belgium*
[3]*Delft University of Technology, Department Radiation, Radionuclides & Reactors, Mekelweg 15, 2629 JB Delft, The Netherlands*

(Received 1 February 2011; accepted 3 April 2011; published online 20 May 2011)

The physical behavior of open-cell foams depends on their microscopic structure. An open-cell geometrical model is proposed, which can serve as the basis for a future macroscopic analysis. The strut geometry is of particular interest, as it is reported to have substantial influence on the occurring thermo-hydraulic and mechanical phenomena. Axial strut size variation, as well as the porosity dependence of shape is quantified and included in a geometrical model. The foam is generated by placing the struts on an elongated tetrakaidecahedron. The required input parameters for the model are two cell dimensions, corresponding to the mean transverse and conjugate diameters of the ellipse encompassing a cell, and the strut cross-sectional surface area at its midpoint between two nodes. The foam geometry is generated iteratively, as porosity is used as validation. A high resolution micro-computed tomography scan is performed to measure the three parameters, the resulting porosity and surface-to-volume ratio. This allows to validate the model. The predictions are found to be within measurement accuracy. A numerical implementation of the model in the preprocessor of a commercial CFD package is demonstrated. © *2011 American Institute of Physics*. [doi:10.1063/1.3587159]

I. INTRODUCTION

Open-cell foams consists of a finite number of polyhedral *cells* where the void space is interconnected through the *pores*. The borders around a pore are termed *struts* or *ligaments* and interconnect the *nodes*, forming a solid matrix which spans the entire porous domain. The nodes are formed where four struts meet, resulting in local metal agglomeration. Open-cell foams are known to exhibit interesting structural and functional properties; the latter due to the open structure:[1]

- High porosity (>90% when uncompressed)
- High specific surface area
- Relatively high strength and toughness, giving them the ability to bear loads
- Good impact energy absorption
- Excellent noise attenuation
- Excellent fluid mixing due to tortuous flow paths
- High gas permeability

The interesting combination of a very light-weight structure with promising functional properties, offers great potential for various applications, such as electro-magnetic radiation shielding,[2] crash energy absorption,[3] rocket jacket cooling,[4] flow conditioner between burner and turbine in jet engines,[5] heat exchangers,[6,7] diesel exhaust cooling,[8] direct tube cooling,[9] biodiesel reactor,[10] hydrogen storage,[11] efficiency enhancement in phase change materials,[12] small-scale refrigerator,[13] high heat flux cooling,[14] electronics heat sinks,[15] LED cooling in automotives,[16] etc. In such applications, foam volumes typically span a vast number of cells. On the other hand, the sub-cell scale phenomena, e.g., fluid flow through the solid matrix or strut buckling during mechanical loading, determine the macroscopic physical response of the material. Due to the complex internal architecture and computational limitations, a microscopic analysis is currently only possible for a limited volume.

For porous media in general, this multi-scale problem can be dealt with by up-scaling the conventional physical laws. The result is that macroscopic properties are introduced, which consider the foam as a superficial material. These physical properties depend on the geometrical characteristics and morphology of the solid matrix. Understanding this dependency requires a detailed definition and measurement of the geometrical parameters, which then can serve to construct a model of the solid matrix. Furthermore, it is desirable to define and use parameters which are controllable during foam manufacturing. This results in feasible optimizations.

The foams studied in this paper are manufactured in house, by replicating a template in aluminum via investment casting.[17] The first step is the preparation of the template by controlling the thickness of a polyurethane preform with a wax layer. The thickening is done by dipping the preform in a molten wax bath and subsequently removing any wax excess. The template is then filled with ceramics and heated. This hardens the ceramic mold and sublimates the template, leaving the negative form of the template in the ceramics. Next the desired metal is cast in this mold under vacuum conditions. After solidification, the mold is removed chemically

[a)]Author to whom correspondence should be addressed. Electronic mail: peter.dejaeger@ugent.be.

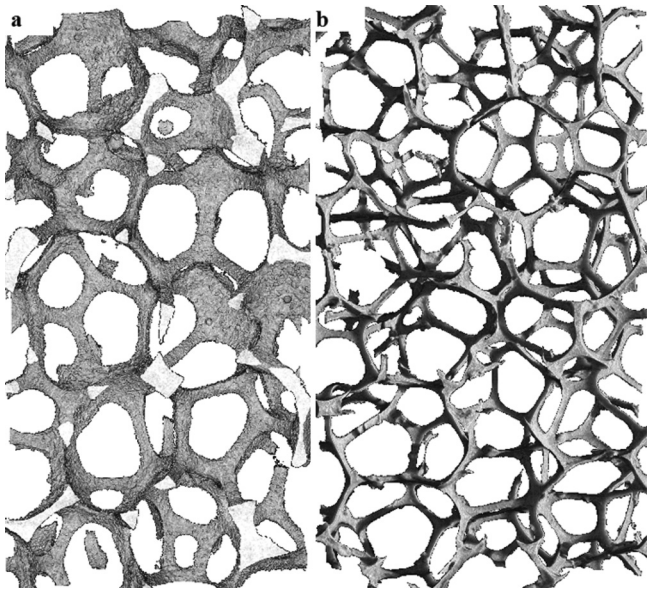

FIG. 1. Microcomputed tomography scan reconstruction of two 20 PPI foams, obtained with 8.5 μm voxel size. Both foams are in-house manufactured and based on the same preform with (a) and without (b) strut thickening.

and/or by high pressure spray and leaves a metal replicate of the template.[18]

The process allows for control of the foam geometry. Cell diameters depend on the choice of polyurethane foam preform, while the thickening procedure alters strut dimensions. This is demonstrated in Fig. 1, where both foams are based on preforms with comparable cell diameters. Thickening with a controlled wax layer has changed porosity from 0.967 to 0.913.

Five foam types were manufactured, which will be discussed in this paper. Note that the employed investment casting process resembles the production method for Duocell® aluminum foam from ERG Materials and Aerospace Corporation. The in-house cast foams have similar features, making the available literature data on ERG foams applicable.

To indicate the type of foam, manufacturers commonly count the number of pores per linear inch (PPI), combined with porosity ϕ or relative density ρ_r.[19] A third important property is the interfacial surface area A_{sf} [m^2] between both phases. Expressing this number per unit volume of porous medium yields the so-called surface-to-volume ratio σ_0 [m^{-1}]. These parameters (PPI, ϕ, and σ_0) alone, have been reported to be inadequate to capture the microscopic behavior of the foam structure. In T'Joen *et al.*,[9] this was experimentally demonstrated by evaluating the thermo-hydraulic performance of screens consisting of round tubes covered with foams of different porosities. Porosity on its own was found to be insufficient to quantify the foam structure; rather the pore diameter and strut diameter should be used. Bonnet *et al.*[20] concluded the same in their study of flow laws in metal foams. Pressure drop related macroscopic properties were found to correlate better with pore diameter than with porosity. The importance of strut cross-sectional area and shape in fluid dynamics is endorsed by the study of Hutter *et al.*[21] By performing a large eddy simulation on isotropic foam models for varying thicknesses and two shapes of the struts, they conclude that the strut shape and thickness seems to be a key parameter to quantify the ability of foam to act as static mixing element, revealing the existence of an optimum. Kanaun and Tkachenko[22] analyzed the influence of strut size variation on effective thermal conductivity. For this macroscopic property, the strut cross-sectional area in the middle between two nodes was found to be a critical parameter. Also, during tension and compression tests, a more detailed characterization of the foam's geometry is required to understand bending, elongation, buckling, and final collapse.[23]

Probably the most accurate foam model can be obtained via microcomputed tomography scan (μCT). However, computational restrictions only allow for limited volumes to be analyzed. These volumes are not sufficient for an analysis of a complete application, but are adequate to derive bulk properties for a macroscopic analysis (see, e.g., Ref. 24). The drawback is that both the μCT and numerical solution techniques are time consuming, limiting the ability to perform parametric studies or optimizations.

The other approach is generating a model, based on the characteristic dimensions of both the solid and liquid phase. For the latter, pore or cell diameters can be used. The pore diameter is easily derived from the PPI count and can be used to approximate a strut length in a cubic cell representation of the solid matrix. However, it is clear that this simplification of the cell structure requires a high degree of empiricism, to correlate derived bulk parameters to experimental data.[25–27] The found results still can deviate substantially from experimental data (see, e.g., Dharmasena and Wadley[28]). A more detailed approach is required.

The objective of this paper is to construct a geometrical model of the foam structure, which can serve in future studies for parametric analysis, optimization, and derivation of macroscopic properties. It is not the intention to capture the microscopic heterogeneous behavior inside the solid matrix.

II. GEOMETRY DESCRIPTION

A. Characterization

Because the structure of the foam is three-dimensional, the pores are not aligned along a single spatial coordinate. Consequently, PPIs are more suited for classifying foam, instead of serving as a geometrical parameter.[29] Porosity is the ratio of the fluid phase to the total foam volume, commonly indirectly determined by measuring the foam's weight and the specific density of the bulk material. Porosity can be measured relatively easy and with great accuracy, with an uncertainty of typically less than 0.2%. It is a macroscopic property which depends on the cell structure and associated dimensions. This makes porosity a suitable parameter to validate potential geometrical models, based on cell and strut dimensions.

Expressing the interfacial surface area per unit mass defines the specific surface area (SSA). SSA can be measured via the Brunauer, Emmet, and Teller (BET) principle, i.e., a technique based on gas adsorption/desorption at the interfacial surface area. The surface-to-volume ratio σ_0 [m^{-1}] is easily

derived from a SSA measurement, via the solid's density. However, the BET method takes the entire surface area in account, down to the nanometer scale.[30] Care should be taken, as not all physical laws are valid at such small scales. For example, fluid flow is based on continuum mechanics, described by the Navier-Stokes equations and no-slip boundary conditions at the fluid-solid interface. For gas flows, this means that the ratio of the mean free path to a characteristic dimension of the solid geometry, i.e., the Knudsen number, is below 0.01.[31] Air, for instance, has a mean free path in the order of 50 nm, meaning that geometrical features below 5 μm should be averaged. As a consequence, surface areas too large for the intended analysis can be obtained via the BET method.[30]

Another method to determine both bulk properties is micro-computed tomography scanning (μCT scan). A virtual, fully three-dimensional model of the foam's structure is reconstructed.[32] The reconstruction of a 20 PPI foam is depicted in Fig. 2. The main difficulty of μCT is image segmentation; i.e., separating between solid and fluid phase. The voxels (3D pixels), which represent the solid matrix boundary, generally consist of both phases. This results in voxels spanning a large range of gray values. Segmentation is about setting the limit to categorize a gray value either as solid (1) or fluid (0). This is done by combining a so-called dual threshold with a labeling operation. Voxels belonging to an interval of gray values are not directly segmented. Instead, they are further processed by identifying subsets of interconnected voxels, which are subsequently assigned to a phase. This is implemented in a code called Morpho+ (see Vlassenbroeck *et al.*[32]) and used in this work. However, it still can lead to significant differences, which can be seen by decreasing the voxel size. The difference between a relatively low and high resolution scan is shown in Fig. 2. The low resolution is a smoothed version of the high resolution scan because the former acts as a low pass filter. The fast changing geometrical features, i.e., spatially high frequency components, are not captured while the high resolution scan clearly shows more detail. This inevitably affects the surface-to-volume ratio. For the low and high resolution scan of Fig. 2, σ_0 increased from 720 to 860 m^{-1}, respectively. This considerable difference of nearly 20% makes voxel size a major parameter when μCT scan data is used. Schmierer and Razani[29] used voxel sizes of 115, 84, 73, and 58 μm, revealing that surface-to-volume ratio converged asymptotically with decreasing voxel size. With the earlier introduced restriction on minimal voxel size, for the continuum assumption to be valid, it is obvious that the high resolution scan can be considered most accurate. The drawback, however, is that it can only be applied to a limited volume due to computer hardware restrictions. To ensure scan volume independence, i.e., that a representative elementary volume (REV) is used, two different volume sizes were analyzed. Notice the surface roughness in the high resolution scan, resulting from the ceramics during manufacturing of the foam.

It is worth mentioning that geometrical analysis also can be done via scanning electron microscopy (SEM).[23,33] In this method, foam samples are prepared by filling them with a resin, i.e., cold mounting, and are subsequently polished. The polished side is reviewed under SEM, allowing for the performance of image analysis. The results are in excellent agreement with those obtained via μCT scan.

Surface-to-volume ratio data of five samples, obtained via a high resolution μCT scan with 8.5μm voxel size, is added to μCT scan data obtained with voxel sizes of 58 μm[29] and 21.8 μm,[35] and the SEM data.[33] Relatively good agreement is found between these data sets. The result is depicted in Fig. 3, clearly showing a systematically higher σ_0 for the data obtained via the BET method,[34] as is expected. In order for the continuum assumption to be valid for air saturated foams, i.e., geometrical features below 5 μm have to be averaged, it is clear that the 8.5 μm voxel size resolution results in relevant data. As can be expected, surface-to-volume ratio increases with decreasing porosity and decreasing PPI number.

B. Cell representation and characteristic dimensions

Models based on spatial tessellation techniques take the inherently stochastic nature of foams into account. Most commonly applied is a random Voronoi tessellation of space (Poisson Voronoi, hard core point process Voronoi, etc.). In principle, it allows for a set of randomly distributed seeds to

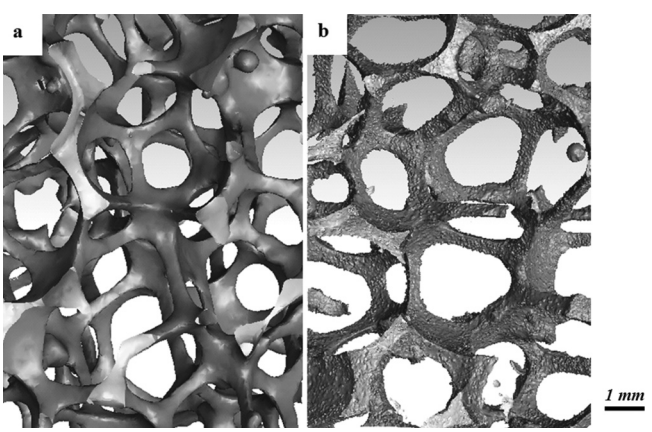

FIG. 2. μCT scan reconstruction of a 20 PPI foam, from (a) a low resolution scan with 40 μm voxel size and (b) a high resolution scan with 8.5 μm voxel size.

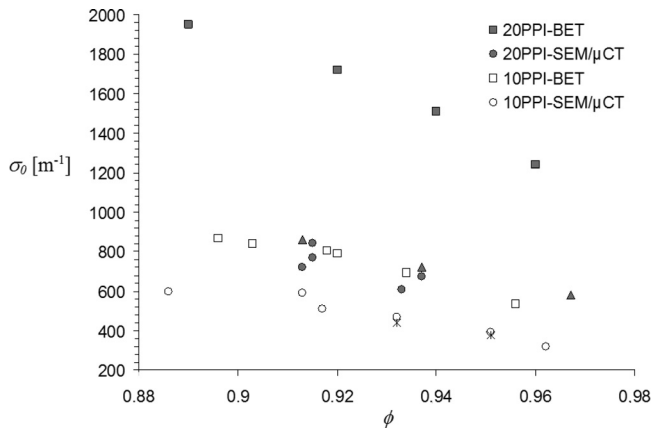

FIG. 3. Surface-to-volume ratio data for 10 and 20 PPI foams, measured via BET,[34] SEM,[33] and μCT scan from literature,[29,35] and of the in-house manufactured 10 PPI (∗) and 20PPI (Δ) foams.

grow simultaneously at controlled rates, until neighboring cells meet. However, the resulting Voronoi tessellations do not show the high degree of regularity that is found in the foam's cell structure; nor does it show the tendency to form pentagonal faces.[36] For these reasons, a weighted generalization of the Voronoi model, i.e., the Laguerre tessellation, is required.[37] Indeed, foams tend to be microscopically heterogeneous, but homogeneous on a macroscopic scale. A quantification of the latter is possible by expressing the standard deviation of characteristic cell dimensions, for a statistical relevant number of cells, as a coefficient of variation (CV). Based on μCT scan analysis, CV values as low as 3.29% and 5.83% for 6 cells of a 10 PPI foam and 5 cells of 20 PPI foam are reported, respectively.[35] This suggests the possibility of representing the foam structure as a periodic reproduction of a unit cell; at least when a macroscopic analysis is intended, or for the derivation of macroscopically averaged properties. Note that analyzing a periodic unit cell (PUC) representation has the advantage that the up-scaled physical equations can be derived from the averaged values of a single unit cell.[38] For stochastic structures, on the other hand, a sufficient number of cells is required, which demands substantial computational capacity.

A deterministic approach to obtain a PUC is based on minimizing the total film energy of the surface between solid and fluid phase. The result is a relaxed version, i.e., smoothed to obtain minimized energy, of a given structure. The SURFACE EVOLVER program[39,53] is developed to tackle this minimization problem, under a given set of constraints (e.g., equal cell volume, fixed nodes in space). The result is an equilibrium foam.[40] This approach can be used to study the well-known Kelvin problem, described as,"finding the minimal surface area partition of three-dimensional space into cells of equal volume." Sir William Thomson[41], Lord Kelvin, proposed a tiling by truncated octahedra with slightly curved faces, i.e. a tetrakaidecahedron formally known as the Kelvin cell. With more modern techniques, it is found that relaxing a Voronoi tessellation, with the seeds placed on a bcc lattice, yields cells which are identical to the Kelvin cell. A 0.03% more efficient unit cell, referred to as WP cell, was found by Weaire and Phelan,[42] after relaxing a space partition with seeds placed on an A15 lattice.

For a foam generated with WP cells, the averaged cell volume and diameter is found to be in close agreement with the values of the original structure,[36] despite not showing the natural tendency to mainly form pentagonal faces.[43] This, and the discussed macroscopic homogeneity of foams, validates a PUC representation of foam for macroscopic analysis. For the investigation of micro-structural effects on elastic properties, the Kelvin model is found to predict the elastic moduli with good accuracy; within 7% on average.[44] The same holds for fluid flow, where periodic single-cell representations allow prediction of pressure drop and even turbulence levels within 5% accuracy.[21] Aiming at a computationally efficient model, previous analysis motivates the selection of a single-unit cell, and more particularly a tetrakaidecahedron, for a PUC representation of the foam structure.

Another aspect which should be considered is the typical unidirectional cell elongation observed in foams. This

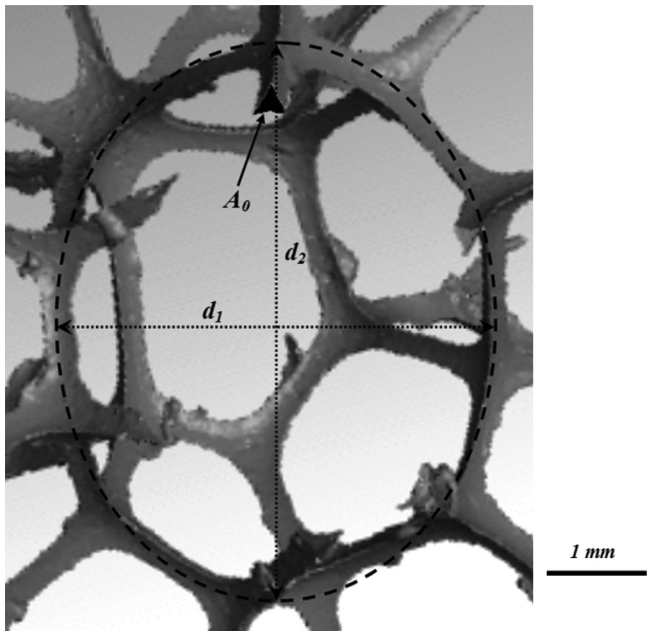

FIG. 4. Geometrical parameter definitions on a μCT scan reconstructed version of the in-house manufactured 20 PPI foam with $\phi = 0.967$. Note the elongated cell structure.

requires two cell diameters, corresponding to the mean conjugate d_1[m] and transverse d_2[m] diameters of the ellipse (illustrated in Fig. 4). To characterize the cell diameters via the earlier introduced Morpho+ software, the individual cells need to be identified. After labeling the void space, a Euclidean distance map is calculated which determines for each point the closest distance to a strut. This allows for separation of the void space in different cells, using a watershed separation algorithm on the distance map. To determine the cell diameters, the largest inscribed sphere in a cell results in the conjugate diameter, while the smallest sphere encompassing the cell allows determination of the transverse diameter. Zhou *et al.*[23] and Perrot *et al.*[35] measured both cell diameters with SEM and μCT scans, respectively, providing consistent data. The ratio of the reported diameters (d_2/d_1) is termed sphericity and measures 1.46 on average. Perrot *et al.*[35] investigated the influence of this orthotropicity on the thermal characteristic length, i.e., a bulk property which is a generalization of the hydraulic radius and is calculated as twice the fluid-phase volume divided by the phase interfacial surface area. It was shown that the thermal characteristic length of an orthotropic cell model is $\pm 30\%$ lower than of an isotropic cell representation. However, their data is still systematically more than 30% higher than the experimental data obtained via μCT scan. Their comparison of tetrakaidecahedra models with different strut and node representations suggests another major influence. Indeed, the difference between cylindrical and equilateral-triangular struts is reported to be in the same order as the earlier mentioned deviations. A more detailed representation of the struts is required.

C. Strut representation and characteristic dimensions

The cell structures discussed above are those of so-called dry foams, i.e., extremely thin cell walls and no strut

volumes are considered. A wire-frame representation of these dry foam models is often used to position an equilateral-triangular rod or a cylindrical representation of struts; see, e.g. Ref. 45, resulting in a wet foam. On the other hand, the Surface Evolver is capable of generating wet foams directly. However, its applicability for investment-cast open-cell metal foams is limited as the thickening process does not obey the surface minimization principles. Thickening has the effect of rounding the sharp cross-sectional strut shape of the polyurethane preform, which was also observed by Jang *et al.*[44] Strut cross-sectional shape is known to depend on porosity[27] and clearly is not an equilateral triangle or a circle. This porosity dependency can be quantified via the Heywood circularity factor (HW), defined as the ratio of the strut cross-section perimeter to the equivalent perimeter of a circle with the same surface area. This factor is determined for 10 strut cross sections of the five foams manufactured in house, as well as its uncertainty. Twice the standard deviation was used as the uncertainty for all the experimental data discussed in this paper, as suggested by Moffat.[46] The measurement is done in the middle between the two nodes connected by the strut. The obtained HW factors are added to the available data from the literature.[29] A power function is found to correlate this factor and porosity, as depicted in Fig. 5. This allows quantification of the shape of the strut cross-section.

Strut cross-sectional area also varies along the axial position between the two nodes it connects. Kanaun and Tkachenko[22] took this in account by positioning struts with a parabolic axial shape on an isotropic dry foam. A more detailed study of this axial variation was carried out by Jang *et al.*[44] Three aluminum foams with nearly equal porosity were analyzed by means of μCT scan, with appropriate voxel size (10 μm). It is observed that the averaged and normalized axial cross-sectional area variation, $f(\xi) = A(\xi)/A_0$, seems independent of the foam type and exhibits quartic behavior. A generalized expression for this behavior is given by:

$$f(\xi) = a_2\xi^4 + \xi^2 + 1, \quad \text{with } \xi = \frac{x}{l} \text{ and } -\frac{l}{2} < x < \frac{l}{2}, \quad (1)$$

and where l is the strut length taken between the two nodes it connects. The cross-sectional surface area at the center between these nodes and at the dimensionless axial position ξ are A_0 and $A(\xi)$, respectively. The axial position is represented by the x coordinate and a_2 is the axial shape factor.

Jang *et al.*[44] also characterized the axial variation of polyurethane foams ($\phi = 0.975 \pm 0.0047$). Recalling the manufacturing process, polyurethane preforms are quasireplicated when no thickening is applied. A confirmation is given for the foam depicted in Fig. 1b, where preform and aluminum foam porosity respectively measured 0.972 and 0.967. The axial shape factor for this foam is 96, which is significantly different than that for the aluminum foam ($a_2 = 36$). To further investigate this, 10 struts of each of the five in-house manufactured open-cell aluminum foams are characterized. The resulting averaged axial shape factors are added to both discussed cases from literature[44] and depicted in Fig. 6, as well as their uncertainty. For the two data points from literature, uncertainty is based on a conservative estimate which allows for covering the range of dimensionless surface areas in the reported figures.

Recognizing that the shape factor is independent of cell dimensions, a second-order polynomial seems acceptable to correlate the shape factor a_2 with the foam's porosity ϕ; at least in the case of $\phi > 0.91$. For less porous foams, however, no data is available. When restricting to porosities above 0.88, a constant axial shape factor of 34.72 is assumed, which is the value obtained for $\phi = 0.913$. The resulting correlation is given by:

$$a_2(\phi) = \begin{cases} 34.72 & \text{for } 0.88 \le \phi \le 0.91 \\ 17342\phi^2 - 31809\phi + 14622 & \text{for } \phi > 0.91 \end{cases}. \quad (2)$$

To quantify the size of a strut, various definitions have been used: the average length of an edge,[23] the height of a triangle best fitting the cross section,[35] the height of an equilateral triangle,[47] the equivalent diameter of a circle yielding the same surface area, or the hydraulic diameter.[29] Furthermore, measuring a length scale of a rounded triangle, which varies in the axial direction, is prone to erroneous readings up to a

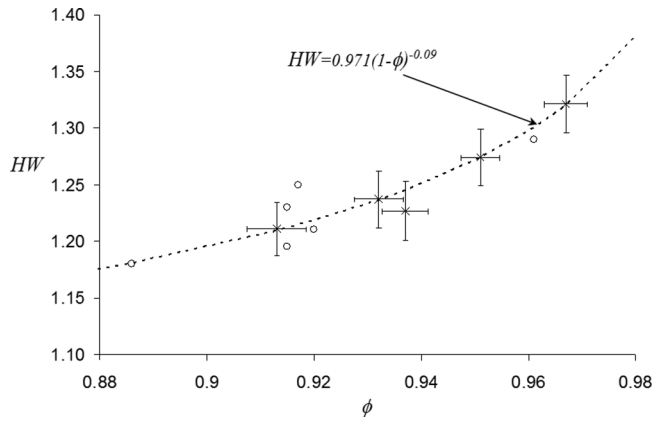

FIG. 5. The porosity-dependent Heywood circularity factor (HW) of the five in-house manufactured foams (∗) is added to the available data from literature (○).[29] A power law is proposed as correlation.

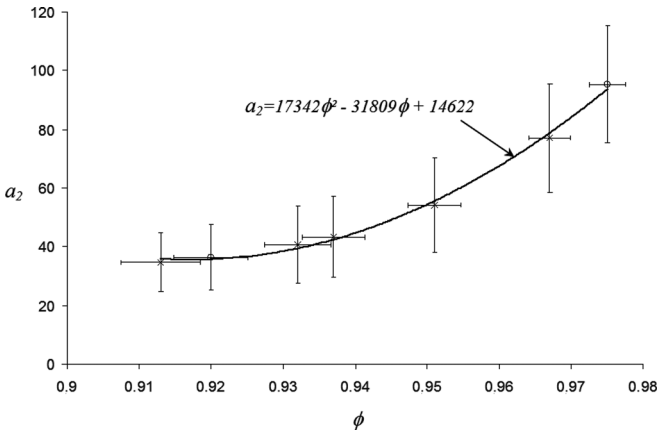

FIG. 6. Axial strut shape factor, correlated with porosity. Data from the five in-house manufactured foams (∗) are added to the two data points from literature,[44] i.e., for a polyurethane and one aluminum foam (○).

factor of two.[48] It is found more convenient to measure the strut cross-sectional surface area and this is also applied in this paper. Measuring at the middle between two nodes gives the least axial variation, making this the favorable location. With the earlier discussed axial strut size and the strut shape dependencies on porosity, it suffices to quantify this surface area A_0 of the strut cross-section at the middle between two nodes.

Now that the appropriate foam parameters are defined, the μCT data of the five in-house manufactured foams can be presented, as well as the data published by Perrot *et al.*[35] The latter is found to be most convenient, because the statistical data of both cell diameters and strut thicknesses is given in detail for 5, 10, 20, and 40 PPI foams. Furthermore, it is found to be in close agreement with the data of Schmierer and Razani[29] and Zhou *et al.*[23] This yields nine open-cell aluminum foam samples, presented in Table I, allowing validation of a geometrical model. The PPI number of the in-house manufactured foams is taken from the polyurethane preform. Notice the spread on the cell diameters for a given PPI number, illustrating their restrictive usefulness.

III. GEOMETRICAL MODEL

The objective is to construct a periodic unit cell representation of the foam structure, based on the three discussed structural characteristics (d_1, d_2, and A_0). Extensive use will be made of both the Heywood circularity factor and axial strut shape factor correlations, in order to grasp the strut's geometry.

A. Cell geometry

As discussed earlier, a tetrakaidecahedron provides sufficient accuracy for the intended macroscopic analysis. An orthotropic wire-frame representation is shown in Fig. 7. The longest struts (l_2) make an angle α with a horizontal plane, which is given by:

$$tg\alpha = \frac{2l_2 \sin\alpha}{d_1 - \sqrt{2}l_1}. \tag{3}$$

Considering a hypothetical isotropic structure allows us to relate l_1 with cell diameter d_1. Indeed, in this hypothetical case, l_1 and l_2 are equally sized and $\alpha = \pi/4$. Putting these conditions in equation (3) yields:

TABLE I. Geometrical data of nine foam samples.

Foam PPI	d_1 [mm]	d_2 [mm]	A_0 [10^{-1} mm^2]	ϕ –	σ_0 [m^{-1}]	Ref. –
10	4.22 ± 0.18	6.23 ± 0.18	0.998 ± 0.08	0.932	440	μCT data
10	4.28 ± 0.13	6.42 ± 0.13	0.615 ± 0.13	0.951	380	μCT data
20	2.52 ± 0.06	3.78 ± 0.06	0.463 ± 0.04	0.913	860	μCT data
20	2.77 ± 0.05	4.15 ± 0.05	0.377 ± 0.05	0.937	720	μCT data
20	2.6 ± 0.05	3.67 ± 0.05	0.126 ± 0.02	0.967	580	μCT data
5	5.2 ± 0.4	6.54 ± 0.55	1.708 ± 0.28[1]	0.918	431	Perrot *et al.*[35]
10	4.1 ± 0.14	6.58 ± 0.50	1.212 ± 0.16[1]	0.918	478	Perrot *et al.*[35]
20	3.26 ± 0.19	4.64 ± 0.41	0.710 ± 0.16[1]	0.917	624	Perrot *et al.*[35]
40	2.78 ± 0.1	3.94 ± 0.31	0.460 ± 0.05[1]	0.923	700	Perrot *et al.*[35]

[1]Values deduced from the published strut thickness distributions.

$$l_1 = \frac{d_1}{2\sqrt{2}}. \tag{4}$$

Consequently, Eq. (3) for the real geometry becomes $tg\alpha = d_2/d_1$. This allows finding an expression for the longer strut in the orthotropic structure, reading:

$$l_2 = \frac{1}{4}\sqrt{d_1^2 + d_2^2}. \tag{5}$$

Both strut lengths are derived from the two characteristic cell diameters, implying that no measurement data of these lengths is required to construct a model. For this reason, strut length is not considered as a foam parameter. Note that the earlier discussed sphericity relates both cell diameters, making only one diameter strictly necessary to generate a wire-frame model of the foam.

B. Strut geometry

The boundary of the strut cross section, in Cartesian coordinates, is given by:[22]

$$\begin{aligned} y(x,\phi) &= R(x)\left(\cos(\phi) + \frac{\cos(2\phi)}{a_1}\right) \\ z(x,\phi) &= R(x)\left(-\sin(\phi) + \frac{\sin(2\phi)}{a_1}\right), \end{aligned} \tag{6}$$

with the angular coordinate varying between $0 \le \phi < 2\pi$ and where the factor $a_1 > 2$ determines the strut shape. The function $R(x)$ defines the changing strut dimension in the axial x direction. The middle of the strut is at $x = 0$. A node is situated at $x = \frac{l}{2}$ or $-\frac{l}{2}$, with l one of the earlier derived strut lengths.

On the basis of Eqs. (6), both the surface area and perimeter of a strut cross section can be derived. These are required

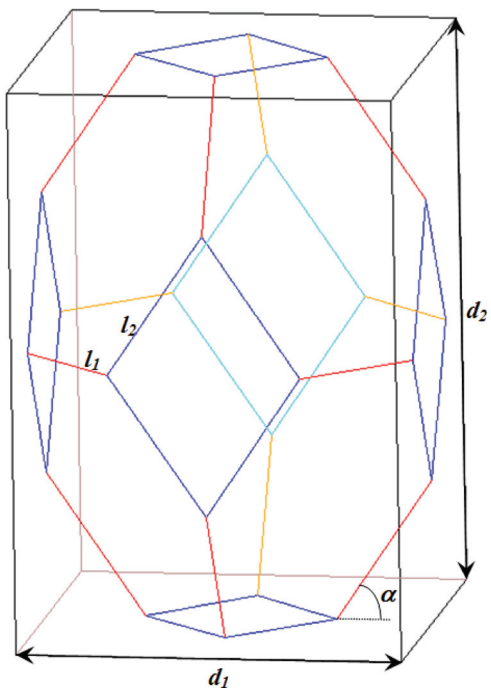

FIG. 7. (Color online) Orthotropic Kelvin cell with straight edges, placed in a REV.

to compute the theoretical Heywood circularity factor, which eventually allows determination of the shape factor a_1.

By applying Green's theorem, i.e., $A = \frac{1}{2}\int_0^{2\pi}\left(z\frac{dy}{d\phi} - y\frac{dz}{d\phi}\right)d\phi$, the cross-sectional surface area of the strut is given by:

$$A(x) = \pi\frac{a_1^2 - 2}{a_1^2}R(x)^2. \tag{7}$$

Note that the strut cross-sectional surface area is less than or equal (in case of $a_1 \to \infty$) to the area of a circle with radius $R(x)$ and, therefore, should not be mistaken for an equivalent radius, which is defined as the radius of a circle yielding the same surface area.

The perimeter is derived by integrating along the contour, after expressing an infinitesimal piece of the contour as $ds = \sqrt{\left(\frac{dy}{d\phi}\right)^2 + \left(\frac{dz}{d\phi}\right)^2}d\phi$, and yields:

$$S(x) = 4R(x)\frac{a_1 - 2}{a_1}E(m), \tag{8}$$

where the function $E(m)$, with $m = -\frac{8a_1}{(a_1-2)^2}$ is the complete elliptic integral of the second kind, given by:

$$E(m) \equiv \int_0^{\pi/2}\sqrt{1 - m^2\sin^2\phi}d\phi. \tag{9}$$

Apart from numerical evaluation, this integral can also be developed in a series:

$$E(m) = \frac{\pi}{2}\left(1 - \sum_{n=1}^{\infty}\left[\frac{(2n-1)!!}{(2n)!!}\right]^2\frac{m^{2n}}{2n-1}\right),$$

allowing an approximation of the perimeter. With this the Heywood circularity factor can be computed, which was earlier correlated with porosity and given by $H(\phi) = 0.971(1-\phi)^{-0.09}$. The result is an expression, relating the shape factor a_1 with porosity ϕ:

$$H(\phi) = \frac{2}{\pi}\frac{a_1 - 2}{\sqrt{a_1^2 - 2}}E(m). \tag{10}$$

This is a transcendental equation, requiring a numerical solution. A simple least-squares minimization algorithm suffices and converges within 10 iterations for a relative residue less than 10^{-6}. The result obtained for three strut shapes is illustrated in Fig. 8 (with $R = 1$), together with the calculated Heywood factor via the rhs of Eq. (10).

Next, an expression of the axial variation function $R(x)$ is required. Equating the generalized shape expression (1) with the normalized strut surface area, given by dividing Eq. (7) with A_0, yields the following expression for the function $R(\xi)$:

$$R(\xi) = a_1\sqrt{\frac{A_0}{\pi(a_1^2 - 2)}f(\xi)}, \tag{11}$$

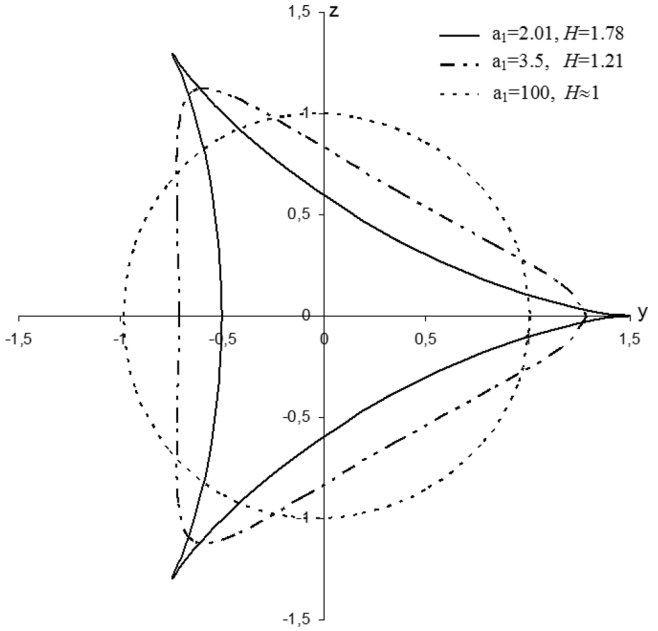

FIG. 8. Three strut cross sections, generated for different shape factors and $R = 1$; with resulting Heywood factor H computed via rhs of Eq. (10).

where $f(\xi)$ is the earlier discussed shape function, which is correlated to the foam's porosity via the axial shape factor a_2 [see Eq. (2)].

C. Porosity and surface-to-volume ratio

To obtain the porosity of the generated structure, the solid content in a representative volume needs to be computed. The first step is integrating the strut cross-sectional surface area along its axial coordinate. The integration limits, however, are not the start and end point of the strut. The strut length needs to be truncated to account for the aluminum accumulation at the nodes. Therefore, it is assumed that a characteristic dimension of a node is given by the axial shape function $f(\xi)$, evaluated in the node ($\xi = -1/2$ or $1/2$). A constant fraction η of the resulting radius is proposed, more particularly: $\frac{\eta}{l}R(1/2)$. The integration limits are subsequently given by $i_1 = -\frac{1}{2} + \eta\frac{R(1/2)}{l}$, and $i_2 = \frac{1}{2} - \eta\frac{R(1/2)}{l}$. The strut volume is determined by integrating:

$$V_{strut} = \int_{i_1}^{i_2} f(\xi)d\xi, \tag{12}$$

where $f(\xi)$ is given by the quartic polynomial of Eq. (1). The truncation fraction is set to $\eta = 1/16$ and is kept constant during the later discussed model validation in Sec. IV.

It is known that, according Plateau's rules, four struts have to meet in a node. For this reason, it is valid to assume that at each strut-end, a strut contributes a quarter of the node volume. Representing this quarter as a tetrahedron allows computation of its volume as:

$$V_{node} = \frac{\sqrt{2}}{3}R(1/2)^2, \tag{13}$$

assuming that twice the radius at the node position is a valid measure for an edge of the tetrahedron. The advantage of this representation is that it allows the quasifit of four struts into one another, although they can have different node-tetrahedra. This is an improved representation, compared to the cubic[45] and spherical[29] node models encountered in literature.

As was noted in Sec II B, it suffices to use the volume of a unit cell as the REV. For the PUC structure, as shown in Fig. 7, this resembles a rectangular box with dimensions d_1, xd_1, xd_2. By determining the total strut volume inside the REV, it is possible to compute the solid content and derive porosity. Recalling that the centerline of a strut is placed along an edge of the wireframe representation, it is clear that not all struts are fully positioned inside the REV. For example, only the upper/lower halves of the eight short struts, i.e., with length l_1, at the bottom/top faces contribute to the solid content in the REV. The 4 other short struts do not coincide with a REV face and therefore are accounted for in full, making a total of 8 short struts with volume $V_{strut_{l_1}}$ active in the REV. Concerning the long struts with length l_2, 16 of them coincide with a REV face and thus only half of them are active. The 8 remaining struts again are fully placed inside the REV, totaling a contribution of 16 long struts with volume $V_{strut_{l_2}}$. The nodes all are positioned half inside the REV. Recalling that the volume of a node is made dependent on the strut size, i.e., $V_{node_{l_1}}$ and $V_{node_{l_2}}$ for struts with length l_1 and l_2, 12 and 24 nodes respectively contribute to the solid content in the REV. The calculated porosity consequently is:

$$\phi = 1 - \frac{8V_{strut_{l_1}} + 16V_{strut_{l_2}} + 12V_{node_{l_1}} + 24V_{node_{l_2}}}{V_{\mathrm{REV}}}. \quad (14)$$

This allows alteration of the strut shape factors iteratively, until porosity is converged. The implemented algorithm is depicted in Fig. 9. Applying it for the nine cases resulted in a maximum of 12 iterations, to obtain a relative porosity difference between the last two iterations of less than 10^{-5}. Note that it is also possible to generate the foam from a known porosity and iterate until the parameter A_0 is converged.

Besides porosity, the surface-to-volume ratio also is of interest. It is obtained by dividing the interfacial surface area with the total REV volume. This surface area is determined by integrating the strut perimeter along the x-coordinate, from i_1 to i_2. The result is given by:

$$A_{sf} = 4\frac{a_1 - 2}{\sqrt{a_1^2 - 2}}\sqrt{\frac{A_0}{\pi}}\int_{i_1}^{i_2}\sqrt{f(\xi)}d\xi, \quad (15)$$

which contains a transcendental integral and has to be treated numerically.

IV. MODEL VALIDATION

To validate the proposed model, calculated and experimental data are compared for the nine cases listed in Table I. Concerning the data of Perrot *et al.*,[35] A_0 had to be deduced from the published distribution of the associated strut thickness. An equilateral-triangular cross-section is assumed,

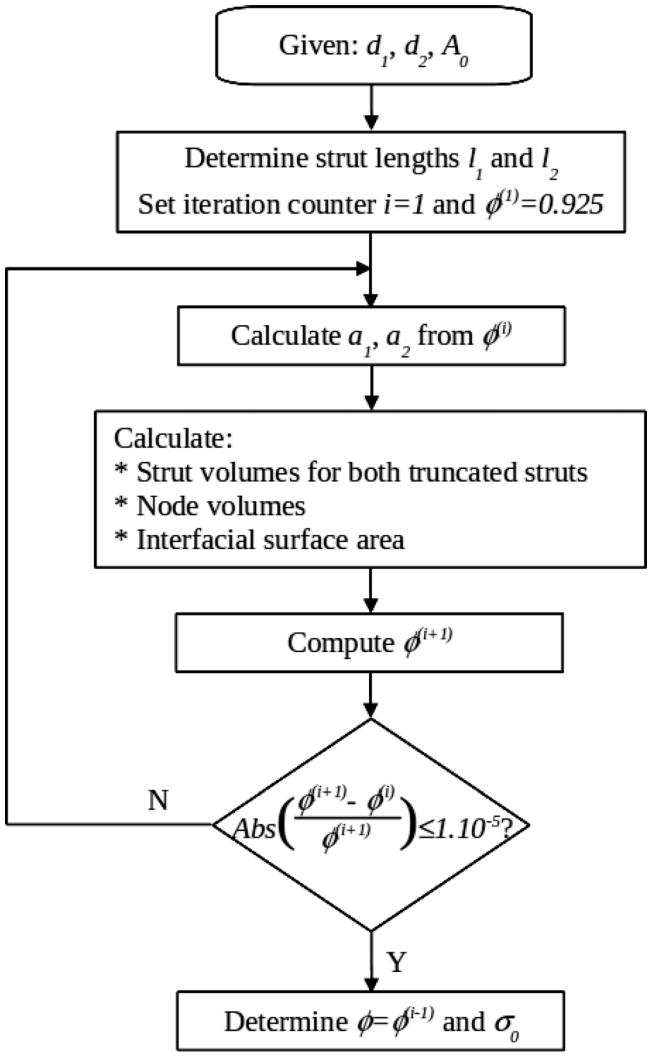

FIG. 9. Iterative procedure to calculate porosity and surface-to-volume ratio for the three given microscopic parameters.

which allows determination of its surface area. A conservative estimate of the uncertainty was made, based on the maximum reported values. This data allows validation of various cell dimensions with nearly constant porosity. For the five μCT data samples, on the other hand, measurement data and uncertainties are directly obtained from the image processing software. Data validity is investigated by analyzing a representative volume, as discussed in Sec. II A. In order to be able to indicate the quality of the calculated results, a thorough uncertainty analysis was performed in accordance with Moffat *et al.*[49] The uncertainties were determined with the root-sum-square method, unless otherwise stated. These five samples have a wider porosity range and thus can be regarded as complementary to the data from literature.

A comparison of the measured and calculated porosity is depicted in Fig. 10, with the obtained uncertainty of both data sets. It is obvious that the calculated porosity and experimental values are in good agreement. A surface-to-volume ratio comparison is shown in Fig. 11, also with calculated and measured results well within their respective uncertainties.

Comparison with the available PUC representations from literature indicates a substantial accuracy improvement.

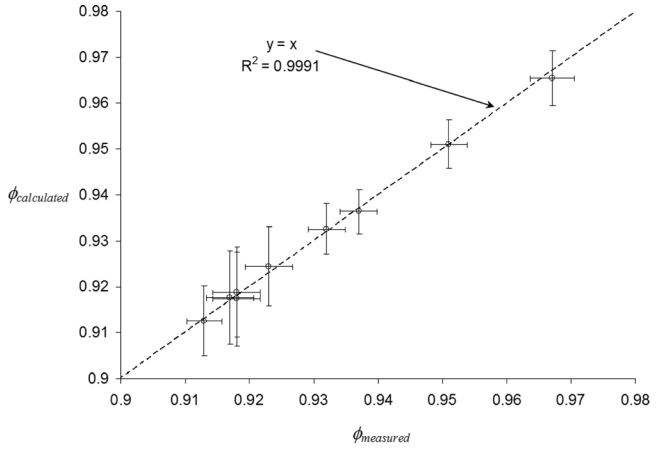

FIG. 10. Model validation: Calculated versus measured porosity for the given geometrical parameters of Table I.

Indeed, Edouard *et al.*[48] reports in a review that available models for foams with porosity above 0.9 yield surface-to-volume ratios with significant deviation. This is verified by depicting in Fig. 11 the surface-to-volume ratio results of the nine foams, obtained with the discussed model and three models from literature.[50–52] The model of Calmidi and Mahajan[51] is based on a cubic cell representation with cylindrical struts and yields results that are systematically too high. Although applying a different modeling approach, both other models overestimate surface-to-volume ratios for experimental values below 550 m^{-1}, find a correct value around $\sigma_0 = 580$ m^{-1}, and underestimate for values above 600 m^{-1}. The main reason for these large spreads is believed to be a combination of measurement accuracy issues and over-simplification of the strut geometry.

The feasibility of using the model for numerical analysis is also investigated. This allows analysis of the averaged microscopic behavior in foam cells. As the Cartesian coordinates are well defined, it is possible to draw a sequence of vertices, which defines the strut boundary. By rigorously drawing the associated edges and faces, it is possible to construct the strut volume via a bottom-up approach. Placing these struts on a wire-frame representation allows for constructing the unit cell. This is implemented in a commercial computational fluid dynamics (CFD) preprocessor, namely Gambit®. The resulting geometry for the first 10 PPI foam, defined in Table I, is shown in Fig. 12. Calculated porosity and surface-to-volume ratio are 0.9326 and 454 m^{-1}, respectively.

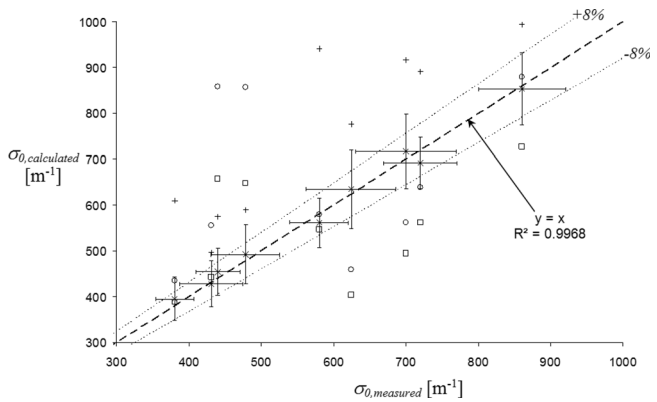

FIG. 11. Model validation: Calculated (∗) versus measured surface-to-volume ratio for the given geometrical parameters of Table I, as well as results obtained with the models of Fourie and Du Plessis[50] (□), Calmidi and Mahajan[51] (+), Giani *et al.*[52] (○).

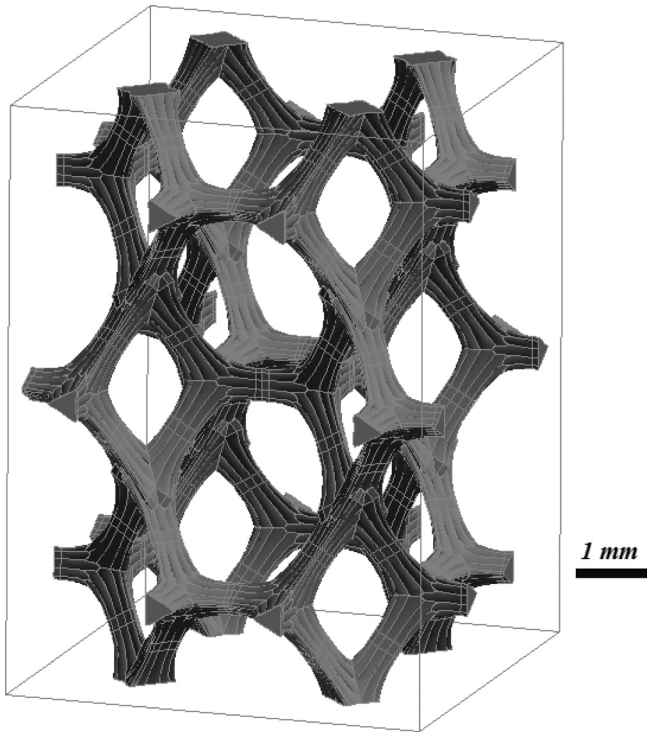

FIG. 12. An orthotropic 10 PPI foam model, with porosity-dependent strut shape and the encompassing rectangular box which forms the REV.

V. CONCLUSION

Studying the influence of structural parameters on physical behavior starts with a sufficiently accurate description of the geometry, which has to be validated experimentally. As currently available models only allow an order of magnitude estimation, more particularly of surface-to-volume ratio, a more detailed approach is derived. To study open-cell aluminum foams on a macroscopic level, a unit cell representation is appropriate, as it is known that the foam structure bears a high degree of regularity on the macroscopic scale.

The model is validated for cast open-cell aluminum foams with porosity higher than 0.88. As both shape factor correlations are derived for these conditions, the model's validity cannot be guaranteed for other manufacturing methods or lower porosities.

The discussed model allows calculation of porosity and surface-to-volume ratio, and generation of a three-dimensional foam geometry, based on three parameters: (i) transverse cell diameters of the elongated cells, (ii) conjugate cell diameters of the elongated cells, and (iii) strut cross-sectional surface area at the middle between two nodes. The advantage is that all three parameters are well-defined and can be obtained with acceptable accuracy, either with SEM or μCT scan analysis. The parameters are furthermore linked to the manufacturing process of the foam, in order to allow optimization of the structure for a given application.

Five foams are analyzed with a μCT scan analysis. The importance of scan resolution is demonstrated. Higher resolution results in more accurate measurements, with significant differences. However, when further analysis is based on the continuum assumption, an appropriate resolution upper limit needs to be respected.

Strut cross-sectional surface area alone is not sufficient to describe the strut geometry. Two additional shape factors are required. The first allows alteration of the strut's cross-sectional shape, and is correlated with porosity. The second factor is a measure of the axial strut size variation, which is also found to depend on porosity. Note that it also allows generation of a foam structure when porosity is given instead of strut cross-sectional surface area. The latter is then derived.

An iterative procedure is implemented to generate the foam structure. The outcome is validated with experimental data, obtained via μCT scan and literature. Good agreement is found, allowing prediction of porosity and surface-to-volume ratio within measurement accuracy, for a given set of parameters.

ACKNOWLEDGMENTS

The authors express their gratitude to Bekaert for the close cooperation. The Institute for the Promotion of Innovation by Science and Technology (IWT Vlaanderen) is greatly acknowledged for their financial support (IWT-090273).

[1]M. F. Ashby, A. Evans, N. Fleck, L. J. Gibson, J. Hutchinson, and H. Wadley, *Metal Foams: A Design Guide* (Butterworth-Heinemann, Woburn, MA, 2000).
[2]O. Losito, PIERS Online **4**, 805 (2008).
[3]A. Jung, H. Natter, S. Diebels, E. Lach, and R. Hempelmann, Adv. Eng. Mater., **13**, 1527 (2010).
[4]R. J. Avenall, "Use of metallic foams for heat transfer enhancement in the cooling jacket of a rocket propulsion element," Master's thesis, University of Florida, Gainesville, FL (2004).
[5]W. Azzi, W. L. Roberts, and A. Rabiei, Mater. Des., **28**, 569 (2007).
[6]S. Y. Kim, J. W. Paek, and B. H. Kang, ASME Trans. J. Heat Transfer **122**, 572 (2000).
[7]J. Klein, N. Arcas, G. Gilchrist, W. Shields, R. Yurman, and J. Whiteside, Technol. Rev. J., **13**, 103 (2005).
[8]S. Mavridou, G. C. Mavropoulos, D. Bouris, D. T. Hountalas, and G. Bergeles, Appl. Therm. Eng. **30**, 935 (2010).
[9]C. T'Joen, P. De Jaeger, H. Huisseune, S. Van Herzeele, N. Vorst, and M. De Paepe, Int. J. of Heat Mass Transfer **53**, 3262 (2010).
[10]X. H. Yu, Z. Z. Wen, Y. Lin, S. T. Tu, Z. D. Wang, and J. Y. Yan, Fuel **89**, 3450 (2010).
[11]S. Mellouli, H. Dhaou, F. Askri, A. Jemni, and S. Ben Nasrallah, Int. J. Hydrogen Energy **34**, 9393 (2009).
[12]K. Lafdi, O. Mesalhy, and S. Shaikh, J. Appl. Phys. **102**, 083549 (2007).
[13]G. B. Ribeiro, J. R. Barbosa, and A. T. Prata, in *Proceedings of 7th World Conference on Experimental Heat Transfer, Fluid Mechanics and Thermodynamics* (AGH University of Science and Technology Press, Krakow, Poland, 2009) p. 483.
[14]B. Agostini, M. Fabbri, J. E. Park, L. Wojtan, J. R. Thome, and B. Michel, Heat Transfer Eng. **28**, 258 (2007).
[15]A. Bhattacharya and R. L. Mahajan, J. Electron. Packag. **124**, 155 (2002).
[16]B. Morkos, P. Shankar, S. Teegavarapu, A. Michaelraj, J. Summers, and A. Obieglo, SAE International Journal of Passenger Cars - Electronic and Electrical Systems **2**, 201 (2009).
[17]J. Banhart, Progress in Material Science **46**, 559 (2001).
[18]D. D. Walz and R. Cordova, *Method of Making an Inorganic Reticulated Foam Structure*, Energy Research Generation (Oakland, CA, 1967).
[19]L. J. Gibson and M. F. Ashby, *Cellular Solids: Structure and Properties*, 2nd ed. (Cambridge University Press, Cambridge, U.K., 1997).
[20]J. P. Bonnet, F. Topin, and L. Tadrist, Transp. Porous Media **73**, 233 (2008).
[21]C. Hutter, A. Zenklusen, S. Kuhn, and P. R. von Rohr, Chem. Eng. Sci., **66**, 519 (2010).
[22]S. Kanaun and E. Tkachenko, Int. J. Eng. Sci. **46**, 551 (2008).
[23]J. Zhou, C. Mercer, and W. Soboyejo, Metall. Mater. Trans. A **33**, 1413 (2002).
[24]J. Hugo, F. Topin, L. Tadrist, and A. Brun, in *Proceedings of the 14th International Heat Transfer Conference* (*IHTC*) (ASME, Washington) 2010 pp. 1–6.
[25]G. Dul'nev, J. Eng. Phys. Thermophys. **9**, 275 (1965).
[26]T. J. Lu, H. A. Stone, and M. F. Ashby, Acta Mater. **46**, 3619 (1998).
[27]A. Bhattacharya, V. V. Calmidi, and R. L. Mahajan, Int. J. Heat Mass Transfer **45**, 1017 (2002).
[28]K. Dharmasena and H. Wadley, J. Mater. Res. **17**, 625 (2002).
[29]E. N. Schmierer and A. Razani, ASME Trans. J. Heat Transfer **128**, 1194 (2006).
[30]K. Sing, D. Everett, R. Haul, L. Moscou, R. Pierotti, J. Rouquerol, and T. Siemieniewska, Pure Appl. Chem. **57**, 603 (1985).
[31]P. Balachandran, *Fundamentals of Compressible Fluid Dynamics* (PHI Learning, New Delhi, 2006).
[32]J. Vlassenbroeck, M. Dierick, B. Masschaele, V. Cnudde, L. Van Hoorebeke, and P. Jacobs, Nucl. Instrum. Methods Phys. Res. A **580**, 442 (2007).
[33]L. Tadrist, M. Miscevic, O. Rahli, and F. Topin, Exp. Therm. Fluid Sci. **28**, 193 (2004).
[34]B. Ozmat, B. Leyda, and B. Benson, Mater. Manuf. Processes **19**, 839 (2004).
[35]C. Perrot, R. Panneton, and X. Olny, J. Appl. Phys. **101**, 1 (2007).
[36]C. Lautensack and T. Sych, Image Analysis and Stereology **25**, 87 (2006).
[37]C. Redenbach, in *Proceedings of the 10th European Congress of Stereology and Image Analysis* (International Society of Stereology, Milano, 2009).
[38]S. Whitaker, *The Method of Volume Averaging* (Kluwer Academic Publishers, Dordrecht, The Netherlands, 1998).
[39]Freely downloadable from: http://www.susqu.edu/brakke/evolver/evolver.html.
[40]R. Phelan, D. Weaire, and K. Brakke, Experimental Mathematics **4**, 181 (1995).
[41]W. Thomson, Sir, Acta Math. **11**, 121 (1887).
[42]D. Weaire and R. Phelan, Philos. Mag. Lett. **69**, 107 (1994).
[43]J. M. Sullivan, NATO ASI Ser., Ser. E **354**, 379 (1998).
[44]W. Jang, A. Kraynik, and S. Kyriakides, Int. J. Solids Struct. **45**, 1845 (2008).
[45]K. Boomsma and D. Poulikakos, Int. J. Heat Mass Transfer **44**, 827 (2001).
[46]R. Moffat, Exp. Therm. Fluid Sci. **1**, 3 (1988).
[47]A. Kopanidis, A. Theodorakakos, E. Gavaises, and D. Bouris, Int. J. Heat Mass Transfer **53**, 2539 (2010).
[48]D. Edouard, M. Lacroix, C. P. Huu, and F. Luck, Chem. Eng. J. **144**, 299 (2008).
[49]R. J. Moffat, J. K. Eaton, and A. Onstad, ASME Trans. J. Heat Transfer **131**, (2009).
[50]J. Fourie and J. Du Plessis, Chem. Eng. Sci. **57**, 2781 (2002).
[51]V. V. Calmidi and R. L. Mahajan, ASME Trans. J. Heat Transfer **122**, 557 (2000).
[52]L. Giani, G. Groppi, and E. Tronconi, Ind. Eng. Chem. Res. **44**, 4993 (2005).
[53]K. Brakke, Exp. Math. **1**, 141 (1992).